IJMMM International Journal of Minerals, Metallurgy and Materials 矿物冶金与材料学报（英文版）

Oxygen variation in titanium powder and metal injection molding

Junping Shen, Chang Liu, Muhammad Dilawer Hayat, Jianan Chen, Hanqing Tian, Fusheng Xin, Gang Chen, Fei Yang, Mingli Qin, and Xuanhui Qu

Cite this article as:
Junping Shen, Chang Liu, Muhammad Dilawer Hayat, Jianan Chen, Hanqing Tian, Fusheng Xin, Gang Chen, Fei Yang, Mingli Qin, and Xuanhui Qu, Oxygen variation in titanium powder and metal injection molding, *Int. J. Miner. Metall. Mater.*, 31(2024), No. 12, pp. 2706-2713. https://doi.org/10.1007/s12613-024-2970-0

View the article online at SpringerLink or IJMMM Webpage.

INTERNATIONAL JOURNAL OF
Minerals, Metallurgy and Materials

Volume 31, Number 12, December 2024
Page 2706

Research Article https://doi.org/10.1007/s12613-024-2970-0

Oxygen variation in titanium powder and metal injection molding

Junping Shen[1),*], *Chang Liu*[1),*], *Muhammad Dilawer Hayat*[2)], *Jianan Chen*[1)], *Hanqing Tian*[1)], *Fusheng Xin*[1)], *Gang Chen*[1,3,4,5),✉], *Fei Yang*[2)], *Mingli Qin*[1,3,4)], *and Xuanhui Qu*[1,4,5)]

1) Beijing Advanced Innovation Center for Materials Genome Engineering, Institute for Advanced Materials and Technology, University of Science and Technology Beijing, Beijing 100083, China

2) School of Engineering, The University of Waikato, Hamilton 3216, New Zealand

3) Institute of Materials Intelligent Technology, Liaoning Academy of Materials, Shenyang 110004, China

4) Beijing Laboratory of Metallic Materials and Processing for Modern Transportation, Beijing 100083, China

5) Ningbo Titan Advanced Materials Technology Co., Ltd., Ningbo 315012, China

(Received: 21 April 2024; revised: 30 June 2024; accepted: 3 July 2024)

Abstract: The control of oxygen is paramount in achieving high-performance titanium (Ti) parts by powder metallurgy such as metal injection molding (MIM). In this study, we purposely selected the Ti and Ti–6Al–4V powders as the reference materials since these two are the most representative Ti materials in the industry. Herein, hydride–dehydride (HDH) Ti powders were pre-oxidized to examine the effect of oxygen variation on the characteristics of oxide layer on the particle surface and its resultant color feature. The results indicate that the thickness and Ti oxide level ($Ti^0 \rightarrow Ti^{4+}$) of the oxide layer on the HDH Ti powders increased as the oxygen content increased, leading to the transition of color appearance from grey, brown to blue. This work aids in the powder feedstock selection at the initial stage in powder metallurgy. In addition, the development of oxygen content was comprehensively studied during the MIM process using the gas-atomized (GA) Ti–6Al–4V powders. Particularly, the oxygen variation in the form of oxide layer, the change of oxygen content in the powders, and the relevant parts were investigated during the processes of kneading, injection, debinding, and sintering. The oxygen variation was mainly concentrated in the sintering stage, and the content increased with the increase of sintering temperature. The variation of oxygen content during the MIM process demonstrates the crucial role of powder feedstock and sintering stage in controlling oxygen content. This work provides a piece of valuable information on oxygen detecting, control, and manipulation for the powder and processing in the industry of Ti and its alloys by powder metallurgy.

Keywords: titanium alloys; oxygen; metal injection molding; powder metallurgy

1. Introduction

Titanium (Ti) and its alloys find extensive applications in aerospace, biomedical, and energy industries owing to their excellent properties such as low density, high strength, excellent corrosion resistance, and good biocompatibility [1–4]. Due to the poor processability of Ti, it is hard to consistently produce complex-shaped, high-performance, and low-cost products of Ti and its alloys through conventional processing technologies e.g., refining casting and extrusion forging [5–8].

Metal injection molding (MIM) is one typical powder metallurgy route that combines powder metallurgy and injection molding technologies [9–11], which excels in producing intricately shaped small to medium-sized parts and is well suited for mass production [12–13]. The application of MIM to produce Ti and its alloys has undergone extensive investigations for several years [9,14], mainly focusing on improving product quality (e.g., densification, size precision, and microstructure) through processing control.

To control the impurity content in Ti and its alloys during powder metallurgy or MIM is of great significance for enhancing the performance of Ti and its alloys. Among the interstitial elements, oxygen has the most significant influence on both microstructure and performance of Ti and its alloys made by powder metallurgy [15−16]. In general, an increased interstitial oxygen content results in strength enhancement while concurrently diminishing the ductility of Ti and its alloys [17–19]. Investigations by Yan *et al.* [20] and Amherd Hidalgo *et al.* [21] explored the correlations between oxygen content, microstructure, and performance for Ti and its alloys. Banerjee and Joens [22] investigated the oxygen content during the sintering stage of MIM, providing insights into potential oxygen sources. These investigations primarily focused on the final products by powder metallurgy, but overlooking the investigations into the original powder. The oxygen source in Ti and its alloys made by powder metallurgy normally comes from the original powder feedstock and oxygen increment during the process. However, variations in the oxygen content of the powder feedstock during powder preparation and throughout the entire MIM process

*These authors contributed equally to this work.

✉ Corresponding author: Gang Chen E-mail: gche098@ustb.edu.cn

(kneading, injection, debinding, and sintering stages) have not been thoroughly studied. Meanwhile, these unexplored investigations play a critical role in understanding the oxygen variation and further possibly providing the oxygen control in powder metallurgy of Ti and its alloys.

This work utilizes the hydride-dehydride (HDH) Ti powders and gas-atomized (GA) Ti–6Al–4V powders as starting materials, to investigate the variation of oxygen content in both preparation of powder feedstock and overall MIM process. In this study, we purposely selected Ti and Ti–6Al–4V powders as the reference materials, since these two are the most widely-used and representative Ti materials in the industry. The findings of this work are able to serve as a valuable reference for the selection of powder feedstock for powder metallurgy, and also fills a gap in understanding the oxygen content variation during MIM for Ti and its alloys.

2. Experimental

2.1. Raw powder

HDH Ti powders, with an irregularly shape (see Fig. 1(a)) and a mean particle size (D_{50}) of 24.4 μm (see Fig. 1(c))), were used for pre-oxidation. Spherical-shaped GA Ti–6Al–4V powders (Fig. 1(b)) with a D_{50} of 17.0 μm were chosen to formulate feedstocks for MIM. Chemical compositions of the HDH Ti and GA Ti–6Al–4V powders are listed in Table 1.

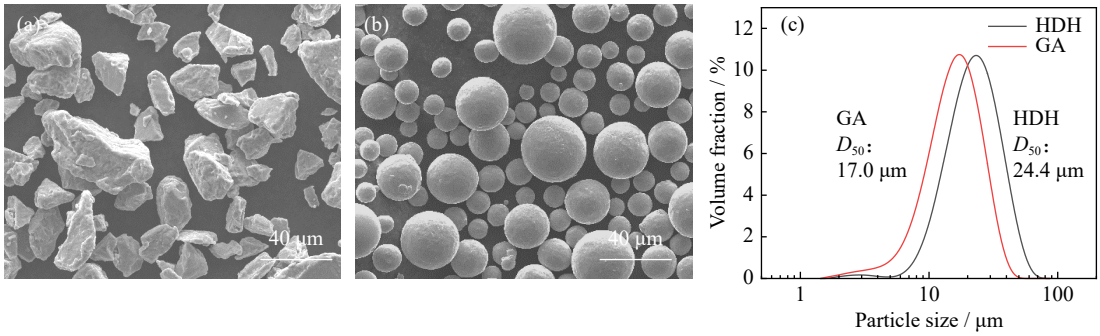

Fig. 1. Microscopic morphologies of the (a) HDH Ti and (b) GA Ti–6Al–4V powders; (c) particle size distribution curves of the HDH Ti and GA Ti–6Al–4V powders.

Table 1. Chemical compositions of the HDH Ti and GA Ti–6Al–4V powders wt%

Powder type	Ti	Al	V	H	N	O	C
HDH	Bal.	—	—	0.027	0.026	0.15	0.059
GA	Bal.	5.94	3.90	0.004	0.017	0.12	0.010

2.2. Powder pre-oxidation and metal injection molding

The pre-oxidation process for the HDH Ti powders was conducted in a quartz tube furnace under a continuous flow of gas mixture (90vol% Ar and 10vol% O_2) under a flow rate at 1 L/min at 350, 400, 450, 500, 550, and 600°C for 30 min, followed by furnace cooling. A multicomponent binder system consisting of paraffin wax (PW), polypropylene (PP), polyethylene (PE), and stearic acid (SA) was used to formulate feedstocks using the GA Ti–6Al–4V powders. Feedstocks were compounded in a mixer (Greenlong M-H-1L-DCSS-H) at 160°C for 2 h at 30 r/min in air. Injection molding was performed on an injection molding machine (Chen Hsong Group, EM80-SVP/2). To conduct solvent debinding, the injection-molded parts were treated in a solvent debinding furnace at 50°C for 12 h, and trichloroethylene was used as the solvent. The debound parts were sintered in a vacuum sintering furnace (BFZS1903111), followed by furnace cooling. We established an experimental group to investigate the effect of sintering profile on the oxygen variation, with specific sintering parameters as outlined in Table 2.

Table 2. Sintering profiles for MIM as functions of temperature and time

No.	Temperature / °C	Time / h
1	1050	5
2	1050	8
3	1150	4
4	1150	5
5	1200	3
6	1250	2
7	1300	2
8	1350	2

2.3. Characterization

A laser particle analyzer (Mastersizer2000) was used to analyze the particle size distribution of the powders. Scanning electron microscopy (SEM, Regulus8100) was used to investigate the microscopic morphologies of the powder and sintered parts. High-resolution transmission electron microscopy (HRTEM, JEM2200FS) was employed to observe the detailed microstructures of the oxide layer. Samples for the oxide layer observation were prepared with a dual-beam focused ion beam system (FIB, FEI Helios NanoLab 600i) using the lift-out technology. The powders (approximately 40 μm in particle size) were sectioned and then deposited with platinum (Pt). The deposited layer's sides were milled using the regular cross-section milling option. Following lift-out, the specimen was further thinned at 30 kV for the oxide layer characterization. The phase identification and surface analysis of the oxide layer were performed by X-ray photoelectron spectroscopy (XPS, Thermo EscaLab 250XI). The alloying contents (aluminum and vanadium) were determined using

an inductively coupled plasma atomic emission spectrometer (Agilent 730 ICP-OES). The oxygen-nitrogen-hydrogen analyzer (TCH600) and carbon-sulfur analyzer (EMIA-820V2) were utilized to analyze the oxygen and carbon contents in the raw powders and sintered parts, respectively. Five measurements were conducted for each type of powder, and the average and standard deviation were then calculated.

3. Results and discussion

3.1. Effect of pre-oxidation on oxygen content of the HDH Ti powders

Pre-oxidation of powders can facilitate the formation of a relatively stable oxide layer on the surface, which exerts a passivation effect and inhibits oxidation reactions [23]. Table 3 lists the oxygen content of the pre-oxidized HDH Ti powders at different temperatures for 30 min, respectively. The oxygen contents of the pre-oxidized powders, with pre-oxidation temperatures ranging from 350 to 600°C, increase from 0.36wt% ± 0.02wt% to 1.04wt% ± 0.02wt%.

Table 3. Oxygen contents of the HDH Ti powders pre-oxidized at different temperatures for 30 min

Temperature / °C	Oxygen content / wt%
Raw powders	0.15 ± 0.02
350	0.36 ± 0.02
400	0.51 ± 0.02
450	0.62 ± 0.02
500	0.79 ± 0.02
550	0.91 ± 0.02
600	1.04 ± 0.02

It has been reported that oxygen in the powders of Ti and its alloys tends to predominantly accumulate on the powder's surface, forming an thin oxide layer [24]. The oxide layer is crystalline, which is mainly composed of TiO_2, Ti_2O_3, and TiO [25–26]. According to literature, the oxygen content within the oxide layer of the powder constitutes a significant proportion of the overall oxygen content at room temperature [26–27]. Therefore, the thickness of oxide layer serves as a crucial indicator for assessing the oxygen content. Fig. 2 shows HRTEM images and corresponding elemental mapping analysis (Ti, Pt, and O) at the interface between the oxide layer and Ti matrix for both raw powder without per-oxidation and the HDH Ti powder pre-oxidized at 350°C for 30 min. The oxide layer thickness increases from (5.9 ± 0.6) nm (Fig. 2(a)) for the raw powders to (17.7 ± 1.8) nm (Fig. 2(b)) for the powders oxidized at 350°C for 30 min. The elemental mapping analysis indicate a significant enrichment of oxygen at the surface of the Ti matrix in the powder oxidized at 350°C for 30 min (Fig. 2(d)) compared to the raw powder (Fig. 2(c)). HRTEM has been widely used to investigate the oxide layer on the powder surface [25–26,28], which has proved to be quite reliable. In addition, the increase in oxide layer thickness indicates a rise in the oxygen content during the pre-oxidation stage, aligning with the observations in Table 3. It demonstrates that the oxide layer thickness on the HDH Ti powder surface increases with the pre-oxidation temperature.

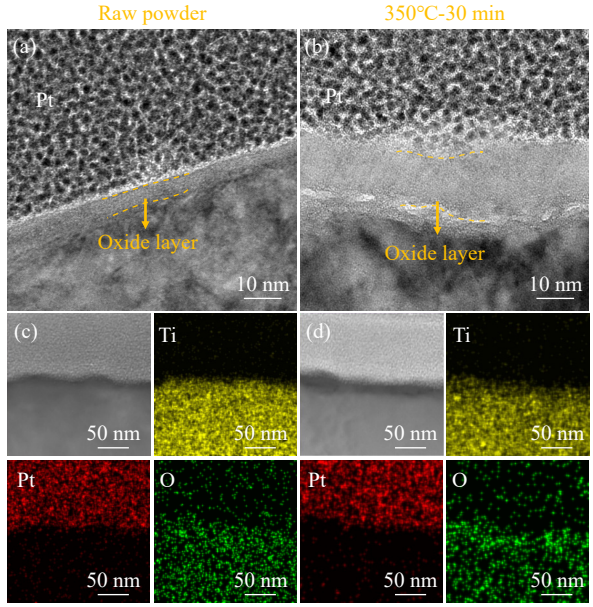

Fig. 2. Microstructural images of the oxide layer of (a) raw HDH Ti powder and (b) pre-oxidized HDH Ti powder and elemental mapping images of (c) raw HDH Ti powder and (d) pre-oxidized Ti powder.

Fig. 3(a)–(c) depicts the peak analysis of Ti 2p spectra for the raw powder and the pre-oxidized HDH Ti powders (pre-oxidized at 350 and 600°C for 30 min). The peak fitting results reveal Ti $2p_{3/2}$ binding energies of (458.6 ± 0.1) eV (Ti^{4+}), (457.2 ± 0.1) eV (Ti^{3+}), (454.1 ± 0.2) eV (Ti^{2+}), and (453.8 ± 0.1) eV (Ti^0), which is consistent with the results in Ref. [29]. The peak analysis indicates the existence of elemental Ti^0 and oxidized Ti^{2+}, Ti^{3+}, and Ti^{4+} within the raw powder. As the temperature rises to 350 and 600°C, the peak analysis indicates the presence of only oxidized Ti^{2+}, Ti^{3+}, and Ti^{4+}. The compositional analysis, as illustrated in Fig. 3(d), elucidates the composition of oxide layer on the raw powder and pre-oxidation powders. In the oxide layer of the raw HDH Ti powder, the content of TiO_2 (Ti^{4+}) is 63.9at%, alongside the presence of Ti_2O_3 (Ti^{3+}), TiO (Ti^{2+}), and elemental Ti (Ti^0). As the temperature rises to 350°C, in the pre-oxidized powders, the TiO_2 content within the oxide layer increases to 83.7at%. Concurrently, there is a reduction in the contents of Ti_2O_3, TiO, and elemental Ti. This suggests a continuous infiltration of oxygen atoms into the substrate, leading to the valence change of Ti from Ti^0 to Ti^{4+}. This gradual transformation ultimately results in the formation of a stable oxide layer. However, after oxidation at 600°C, the TiO_2 content decreases to 54.7at%, while the corresponding contents of Ti_2O_3 and TiO increase. This implies the decomposition of TiO_2 at high temperatures, with oxygen atoms diffusing from the TiO_2 into Ti_2O_3, TiO, and Ti substrate.

Interestingly, as the temperature rises from 25 to 600°C, the observed color development of the HDH Ti powders follows this rule: gray → gold → brown → mauve → dark purple → blue, as shown in Fig. 4(a). During the pre-oxida-

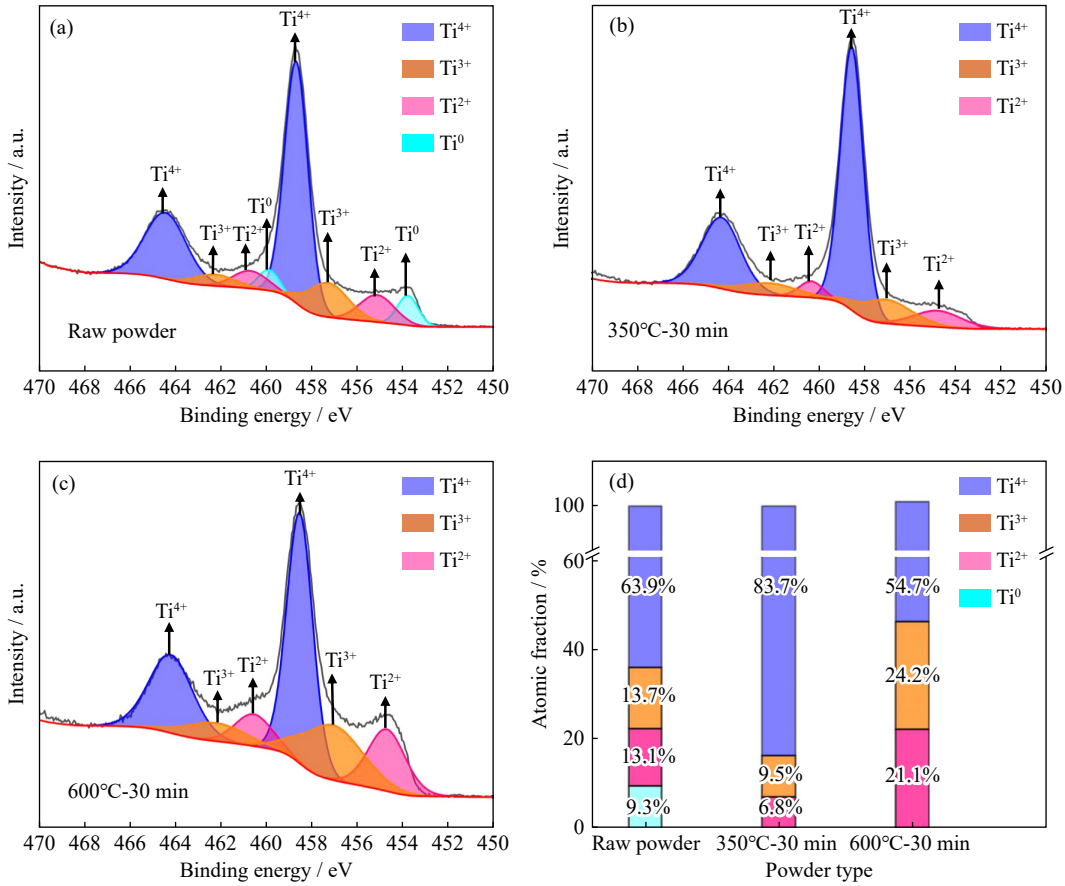

Fig. 3. Peak fittings of Ti 2p spectra on the powder surface: (a) raw HDH Ti powder; (b) HDH Ti powders subjected to pre-oxidation at 350°C for 30 min; (c) HDH Ti powders pre-oxidized at 600°C for 30 min. (d) Compositions of the oxide layer for these powders.

tion stage, the powder color can serve as an indicator of its oxidation degree and/or oxygen content. The color transformation of Ti powder is significantly correlated to its reflectance, primarily influenced by the interference phenomenon resulting from differences in the thickness of oxide layer [30−31]. Fig. 4(b) illustrates the mechanism of color variation in the oxygen layer at different thickness levels. When the powder surface is illuminated, light 1 penetrates the oxide layer and reflects off the underlying metal surface, while light 2 reflects off the oxide layer surface, leading to their convergence into a unified interfering beam. The optial path difference of light 1 and light 2 can be expressed as Eqs. (1) and (2) [31−32]:

$$\Delta = 2d\sqrt{n_m^2 - n_a^2 \times \sin^2 i_0} = \begin{cases} k\lambda, k = 1,2,\cdots \\ (2k+1)\dfrac{k\lambda}{2}, k = 0,1,2\cdots \end{cases} \quad (1)$$

$$n_m = \sum_{i=2}^{4} x_i n_i \quad (2)$$

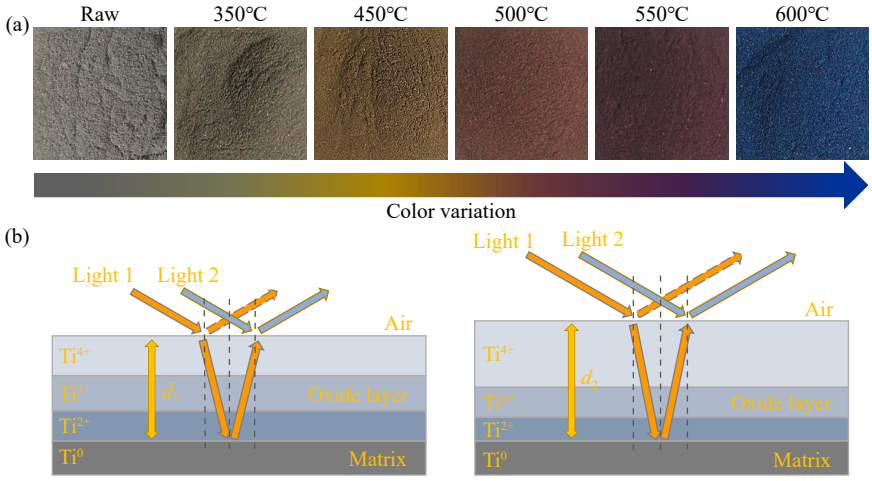

Fig. 4. (a) Color variation of the HDH Ti powders subjected to pre-oxidation for 30 min at different temperatures and (b) schematic diagram illustrating the mechanism of color variation in the oxygen layer at different thickness levels.

where Δ is the optical path difference, i_0 is the angel of incidence of light, λ is the wavelength of light, k is the natural number, d is the thickness of oxide layer, n_a is the refractive index of air, n_m is the mean refractive index of oxide layer, respectively. In formula (1), n_m is composed of $x_i n_i$, where $i = 2$, 3, 4. x_i and n_i are the contents and refractive indices of TiO (Ti^{2+}), Ti_2O_3 (Ti^{3+}), and TiO_2 (Ti^{4+}) in the oxide layer, respectively. The refractive index of TiO [33], Ti_2O_3 [34], and TiO_2 [35] is 2.31, 2.35 and 2.64, respectively. The HRTEM results, as presented in Fig. 2, reveal that the oxide layer thickness of the raw powder is 5.9 nm. With the temperature increasing to 350°C, the oxide-layer thickness increased to 17.7 nm. Peak fittings data demonstrate that within the XPS detection range, as the temperature increased to 350°C, the content of Ti^{4+} in the oxide layer gradually increased, while the contents of Ti^{3+} and Ti^{2+} decreased. Consequently, the average refractive index increased from 2.31 to 2.59. With the temperature further increasing to 600°C, there was a progressive decrease in the content of Ti^{4+} in the oxide layer, while the contents of Ti^{3+} and Ti^{2+} increased, leading to a decrease in the average refractive index to 2.50. As expressed in Eq. (1), when Δ equals to $k\lambda$, the interference enhancement occurs. In addition, the enhancement of certain wavelengths of light waves after interference depends on the oxide layer thickness and refractive index of oxide layer. Such distinctive interference enhancements result in variation of coloration of the HDH Ti powders. Therefore, the coloration of the HDH Ti powders in this study indicates an insight into the oxygen level, which is useful to instantly estimate the oxygen content of Ti and its alloy powders in industry.

3.2. Variation of oxygen content during metal injection molding

In the MIM process of Ti and its alloys, a substantial quantity of binder is introduced with the raw powders to form the feedstock. Accordingly, the temporarily introduced binder will be completely removed through debinding and subsequent sintering, which inevitably increases the risk of oxidation during the entire process. As such, the oxygen control during the feedstock kneading, debinding, and sintering stages within MIM becomes significantly important. With respective to this, characterization of oxygen variation during MIM is immensely critical to fully understand the entire status and further formulate the processing window for MIM of Ti and its alloys.

However, gauging the oxygen variation for the first step of feedstock kneading and solvent debinding is extremely difficult, because the widely-used methodologies such as chemical measuring are not able to correctly determine the oxygen content of powders, due to the abundant mixture of binder polymer. In this study, we innovatively proposed a reliable route to determine the powder oxidation status via comparing the oxide layer of raw and solvent-debound powder (after kneading and solvent debinding). Fig. 5(a) and (b) shows the microstructural images of raw GA Ti–6Al–4V powders and those after solvent debinding. As can be seen from Fig. 5(b), the powder surfaces are wrapped with binder even after solvent debinding. To further investigate the oxygen content of powders after solvent debinding, HRTEM characterization of the oxide layer was performed by comparing the raw and solvent-debound powders (Fig. 5(c) vs. Fig. 5(d)). The average thickness of oxide layer of the raw powder is ca. (3.5 ± 0.4) nm as determined from Fig. 5(c), and it is approximately (3.5 ± 0.3) nm for the solvent-debound powder (see Fig. 5(d)). This result suggests that the powder oxidation during the kneading and solvent debinding stages can be negligible, attributed to the unchanged thickness of oxide layer. This route is reliable because of the following reasons: (1) the oxygen content of powders mainly comes from the oxide layer [24,27]; (2) the kneading and solvent debinding temperatures are well below 200°C when the oxide layer is relatively stable due to the mild oxygen atomic diffusion from the oxide layer into the powder matrix [36−37].

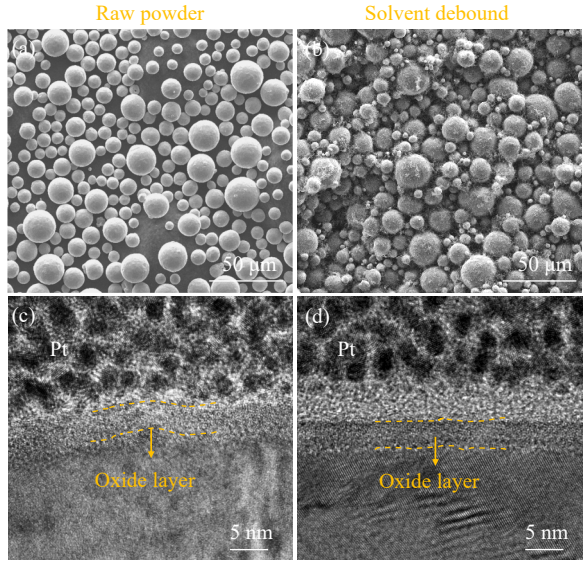

Fig. 5. SEM images of the GA Ti–6Al–4V (a) raw powders and (b) powder after solvent debinding; HRTEM images of the oxide layer for (c) the raw powder and (d) the powder after solvent debinding.

Powder sintering of Ti and its alloys is usually conducted over 1000°C (within the β phase zone), while the oxygen atomic diffusion in the Ti crystal lattice is significantly boosted at such high temperatures, as compared to the kneading and debinding stages. In this work, a comprehensive study on sintering as functions of sintering temperature and holding time was carried out to examine the impact of sintering profile on the oxygen content in the sintered parts. Fig. 6 presents the oxygen contents of the sintered Ti–6Al–4V parts with corresponding sintering parameters (samples 1 to 8 as shown in Table 2). The oxygen contents of samples 1 to 8 gradually increase from 0.15wt% ± 0.01wt% to 0.27wt% ± 0.01wt%. Several points can be drawn from Fig. 6: (1) the oxygen content in the system gradually increases with the sintering temperature from 1050 to 1350°C; (2) the oxygen content increases with the holding time under an identical sintering temperature (samples 1 vs. 2, and samples 3 vs. 4); (3) it indicates that the sintering temperature plays a prior role in the oxygen increment, since the oxygen content of sample 1 (sintering at 1050°C for 5 h) is much lower than that of

sample 8 (sintering at 1350°C holding for 2 h). This indicates that sintering is the primary stage to raise the oxidation risk during MIM in terms of sintering temperature and holding time.

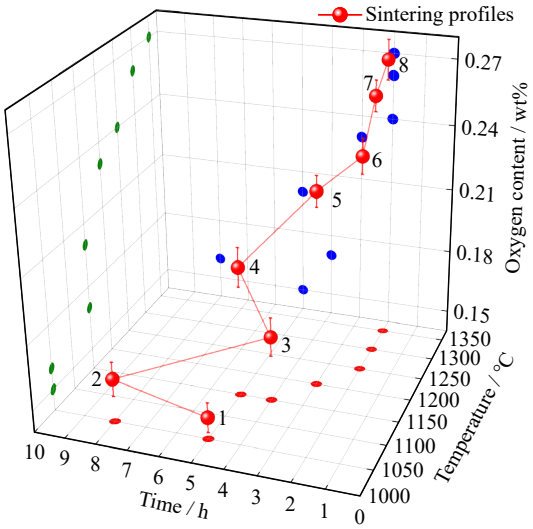

Fig. 6. Oxygen contents of the sintered Ti–6Al–4V parts with corresponding sintering profiles for MIM.

In addition, the oxide layer begins to dissolve when the sintering temperature increases to a critical point such as 500°C for Ti powders concomitant with the sintering necking among nearby powders [38]. After sintering at 1050–1350°C, the oxygen atoms in the oxide layer have completely dissolved into the matrix, resulting in the oxygen atoms uniformly distributed in the sample. In such a case, the oxide layer is absent in the sintered sample and cannot be observed using either SEM or TEM. Only equiaxed grains (see Fig. 7(a)) and typical Widmanstätten microstructures (see Fig. 7(b)–(f)) are present.

In this study, the variation in oxygen content during the MIM process is typically associated with the oxygen atomic diffusion, which is governed by thermodynamics and kinetics [39]. The increase of oxygen content, as presented in Fig. 6, can be explained through the oxygen atomic diffusion by the Arrhenius Eq. [40]:

$$K = A\exp\left(\frac{-E_a}{RT}\right) \tag{3}$$

where K is the diffusion coefficient, A is the diffusion constant, E_a is the diffusion activation energy, R is the molar gas constant, and T is the temperature in Kelvin, respectively. According to the Eq. (3), the diffusion coefficient is dependent on temperature, which rises with increasing the temperature. During the sintering stage under vacuum, the vacuum furnace inevitably harbors a trace of impurities originating from the furnace and residual binder, thereby regarded as a source of oxygen [22]. The stability of oxygen atom within the oxide layer is inferior to that within the Ti matrix, driven by which the apparent oxide-layer dissolution into the matrix takes place at 500°C [38]. Oxygen atoms undergo diffusion from the outermost TiO_2 layer towards the matrix, finally leaving behind a concentration gradient. Exposed Ti atoms on the surface significantly raise the surface chemical activity and concurrently diminish the activation energy required for the atomic diffusion [23]. Generally, the increase of sintering temperature leads to the corresponding increase of the oxygen atomic diffusion coefficient, causing the accelerated migration of oxygen atom and weakening of the obstructive effect of the oxide layer [38,41]. Similarly, either elevating the sintering temperature or prolonging the holding time result in the increment of atomic diffusion and thus the increase of oxygen content, as evidenced in Fig. 6. Thus, formulating and optimizing the sintering window is particularly crucial in oxygen control for MIM of Ti and its alloys.

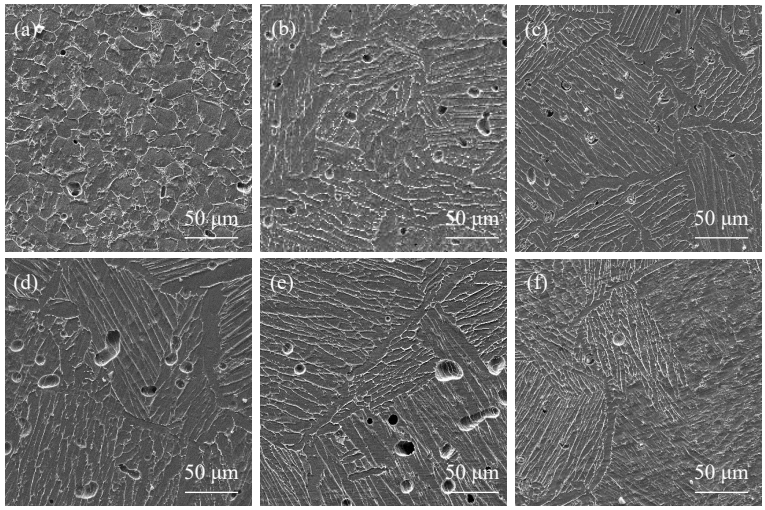

Fig. 7. SEM images of the sintered samples after sintering at different temperatures and holding time: (a) 1050°C-5 h; (b) 1050°C-8 h; (c) 1150°C-5 h; (d) 1200°C-3 h; (e) 1250°C-2 h; (f) 1300°C-2 h.

4. Conclusions

This study covers the entire process on the oxygen level and oxidation feature of the powder and sintered parts, which provides valuable guidance for the Ti and its alloys in the powder metallurgy industry involving both Ti and Ti–6Al–4V alloy systems. Following points can be summarized.

(1) In the pre-oxidation process, the oxygen content increases with the pre-oxidation temperature. Besides, the transition of color appearance for the HDH Ti powders is determined by the oxide layer on the powder surface in terms of thickness and chemical composition.

(2) Through the observation of oxide layer thickness, the oxidation of GA Ti–6Al–4V powders is minimal after kneading with binder and subsequent solvent debinding during MIM.

(3) Within the sintering stage during MIM, the oxygen content of the sintered parts using the GA Ti–6Al–4V powders gradually increases with the sintering temperature and holding time increasing, due to the correspondingly increased atomic diffusion coefficient. Notably, the impact of sintering temperature is more prominent than that of holding time.

Acknowledgements

This study was financially supported by the National Key Research and Development Program of China (No. 2021YFB3701900), the National Natural Science Foundation Program of China (No. 51971036), and the Open Research Fund of State Key Laboratory of Mesoscience and Engineering (No. MESO-23-D07).

Conflict of Interest

Xuanhui Qu is an editorial board member for this journal and was not involved in the editorial review or the decision to publish this article. The authors have no competing interests to declare that are relevant to the content of this article.

References

[1] W.S. Lee and C.F. Lin, Plastic deformation and fracture behaviour of Ti–6Al–4V alloy loaded with high strain rate under various temperatures, *Mater. Sci. Eng. A*, 241(1998), No. 1-2, p. 48.

[2] X.W. Ji, P.T. Liu, J.C. Tang, *et al*., Different antibacterial mechanisms of titania nanotube arrays at various growth phases of E. coli, *Trans. Nonferrous Met. Soc. China*, 31(2021), No. 12, p. 3821.

[3] J.P. Zheng, L.J. Chen, D.Y. Chen, C.S. Shao, M.F. Yi, and B. Zhang, Effects of pore size and porosity of surface-modified porous titanium implants on bone tissue ingrowth, *Trans. Nonferrous Met. Soc. China*, 29(2019), No. 12, p. 2534.

[4] G.Z. Qiu and Y.F. Guo, Current situation and development trend of titanium metal industry in China, *Int. J. Miner. Metall. Mater.*, 29(2022), No. 4, p. 599.

[5] G.C. Obasi, O.M. Ferri, T. Ebel, and R. Bormann, Influence of processing parameters on mechanical properties of Ti–6Al–4V alloy fabricated by MIM, *Mater. Sci. Eng. A*, 527(2010), No. 16-17, p. 3929.

[6] S. Sun, M. Brandt, and M.S. Dargusch, Characteristics of cutting forces and chip formation in machining of titanium alloys, *Int. J. Mach. Tools Manuf.*, 49(2009), No. 7-8, p. 561.

[7] Y. Gao, C. Zhang, J.Z. Zhang, and X. Lu, Microstructure evolution and strengthening mechanism of high-performance powder metallurgy TA15 titanium alloy by hot rolling, *Int. J. Miner. Metall. Mater.*, 31(2024), No. 6, p. 1426.

[8] L. Lan, R.Y. Xin, X.Y. Jin, S. Gao and B. He, Influence of multiple laser shock peening treatments on the microstructure and mechanical properties of Ti–6Al–4V alloy fabricated by electron beam melting, *Int. J. Miner. Metall. Mater.*, 29(2022), No. 9, p. 1780.

[9] F.H.S. Froes, Advances in titanium metal injection molding, *Powder Metall. Met. Ceram.*, 46(2007), No. 5, p. 303.

[10] R.M. German, Progress in titanium metal powder injection molding, *Materials*, 6(2013), No. 8, p. 3641.

[11] A. Dehghan-Manshadi, M. Bermingham, M.S. Dargusch, D.H. StJohn, and M. Qian, Metal injection moulding of titanium and titanium alloys: Challenges and recent development, *Powder Technol.*, 319(2017), p. 289.

[12] E. Ergül, H. Özkan Gülsoy, and V. Günay, Effect of sintering parameters on mechanical properties of injection moulded Ti–6Al–4V alloys, *Powder Metall.*, 52(2009), No. 1, p. 65.

[13] L. Liu, X.D. Wang, X. Li, X.T. Qi, and X.H. Qu, Effects of size reduction on deformation, microstructure, and surface roughness of micro components for micro metal injection molding, *Int. J. Miner. Metall. Mater.*, 24(2017), No. 9, p. 1021.

[14] S. Virdhian, T. Osada, H.G. Kang, F. Tsumori, and H. Miura, Evaluation and analysis of distortion of complex shaped Ti–6Al–4V compacts by metal injection molding process, *Key Eng. Mater.*, 520(2012), p. 187.

[15] Y.J. Liu, Y. Pan, J.Z. Sun, *et al*., Metal injection molding of high-performance Ti composite using hydride-dehydride (HDH) powder, *J. Manuf. Process.*, 89(2023), p. 328.

[16] X.M. Gan, S.F. Li, S.Y. Xiao, and Y.F. Yang, Integrated high-performance and accurate shaping technology of low-cost powder metallurgy titanium alloys: A comprehensive review, *Int. J. Miner. Metall. Mater.*, 31(2024), No. 3, p. 413.

[17] H. Conrad, Effect of interstitial solutes on the strength and ductility of titanium, *Prog. Mater. Sci.*, 26(1981), No. 2-4, p. 123.

[18] T. Ebel, O. Milagres Ferri, W. Limberg, M. Oehring, F. Pyczak, and F.P. Schimansky, Metal injection moulding of titanium and titanium-aluminides, *Key Eng. Mater.*, 520(2012), p. 153.

[19] H. Wang, Q. Chao, X.Y. Cui, *et al*., Introducing C phase in additively manufactured Ti–6Al–4V: A new oxygen-stabilized face-centred cubic solid solution with improved mechanical properties, *Mater. Today*, 61(2022), p. 11.

[20] M. Yan, M.S. Dargusch, T. Ebel, and M. Qian, A transmission electron microscopy and three-dimensional atom probe study of the oxygen-induced fine microstructural features in as-sintered Ti–6Al–4V and their impacts on ductility, *Acta Mater.*, 68(2014), p. 196.

[21] A. Amherd Hidalgo, T. Ebel, R. Frykholm, E. Carreño-Morelli, and F. Pyczak, High-oxygen MIM Ti–6Al–7Nb: Microstructure, tensile and fatigue properties, *Mater. Today Commun.*, 34(2023), art. No. 104982.

[22] S. Banerjee and C.J. Joens, Sintering powder metal injection molded (MIM) titanium alloys: In vacuum or argon?, *Key Eng. Mater.*, 704(2016), p. 113.

[23] F.S. Xin, W.W. Ding, Q.Y. Tao, *et al*., Effect and evolution of oxide film in the HDH-Ti powder surface on densification behavior during sintering, *Metall. Mater. Trans. A*, 53(2022), No. 4, p. 1164.

[24] Q.Y. Tao, Z.W. Wang, G. Chen, *et al*., Selective laser melting of CP-Ti to overcome the low cost and high performance trade-off, *Addit. Manuf.*, 34(2020), art. No. 101198.

[25] Q.Y. Tao, W.W. Ding, G. Chen, X.H. Qu, and M.L. Qin, Towards an atomic-scale understanding of oxide film in the Ti powder surface, *Scripta Mater.*, 210(2022), art. No. 114471.

[26] W.W. Ding, Z.W. Wang, G. Chen, *et al*., Oxidation behavior of low-cost CP-Ti powders for additive manufacturing *via* fluidization, *Corros. Sci.*, 178(2021), art. No. 109080.

[27] E. Hryha, R. Shvab, M. Bram, M. Bitzer, and L. Nyborg, Surface chemical state of Ti powders and its alloys: Effect of storage conditions and alloy composition, *Appl. Surf. Sci.*, 388(2016), p. 294.
[28] S. Mendis, W. Xu, H.P. Tang, *et al*., Characteristics of oxide films on Ti–(10–75)Ta alloys and their corrosion performance in an aerated Hank's balanced salt solution, *Appl. Surf. Sci.*, 506(2020), art. No. 145013.
[29] M.C. Biesinger, L.W.M. Lau, A.R. Gerson, and R.S.C. Smart, Resolving surface chemical states in XPS analysis of first row transition metals, oxides and hydroxides: Sc, Ti, V, Cu and Zn, *Appl. Surf. Sci.*, 257(2010), No. 3, p. 887.
[30] R. Williams, M. Bilton, N. Harrison, and P. Fox, The impact of oxidised powder particles on the microstructure and mechanical properties of Ti–6Al–4V processed by laser powder bed fusion, *Addit. Manuf.*, 46(2021), art. No. 102181.
[31] M.V. Diamanti, B. Del Curto, and M. Pedeferri, Interference colors of thin oxide layers on titanium, *Color Res. Appl.*, 33(2008), No. 3, p. 221.
[32] M.H. Freeman, *Optics*, Elsevier, Amsterdam, 1990.
[33] E.M. Assim, Optical constants of titanium monoxide TiO thin films, *J. Alloys Compd.*, 465(2008), No. 1-2, p. 1.
[34] M.M. Abdel-Aziz, I.S. Yahia, L.A. Wahab, M. Fadel, and M.A. Afifi, Determination and analysis of dispersive optical constant of TiO_2 and Ti_2O_3 thin films, *Appl. Surf. Sci.*, 252(2006), No. 23, p. 8163.
[35] J.R. DeVore, Refractive indices of rutile and sphalerite, *J. Opt. Soc. Am.*, 41(1951), No. 6, p. 416.
[36] P.A. Lee, K.F. Stork, B.L. Maschhoff, K.W. Nebesny, and N.R. Armstrog, Oxide formation on Fe and Ti thin films and on Fe thin films modified with ultrathin layers of Ti, *Surf. Interface Anal.*, 17(1991), No. 1, p. 48.
[37] I. Vaquila, M.C.G. Passeggi, and J. Ferrón, Temperature effects in the early stages of titanium oxidation, *Appl. Surf. Sci.*, 93(1996), No. 3, p. 247.
[38] C. Jiménez, F. Garcia-Moreno, B. Pfretzschner, *et al*., Decomposition of TiH_2 studied *in situ* by synchrotron X-ray and neutron diffraction, *Acta Mater.*, 59(2011), No. 16, p. 6318.
[39] E.W. Lui, S. Palanisamy, M.S. Dargusch, and K. Xia, Oxide dissolution and oxygen diffusion in solid-state recycled Ti–6Al–4V: Numerical modeling, verification by nanoindentation, and effects on grain growth and recrystallization, *Metall. Mater. Trans. A*, 48(2017), No. 12, p. 5978.
[40] S. Arrhenius, Über die Reaktionsgeschwindigkeit bei der inversion von rohrzucker durch säuren, *Z. Phys. Chem.*, 4U(1889), No. 1, p. 226.
[41] Z. Liu and G. Welsch, Literature survey on diffusivities of oxygen, aluminum, and vanadium in alpha titanium, beta titanium, and in rutile, *Metall. Trans. A*, 19(1988), No. 4, p. 1121.